Environ Earth Sci (2012) 67:889–910
DOI 10.1007/s12665-012-1537-y

ORIGINAL ARTICLE

Integrated geophysics and soil gas profiles as a tool to characterize active faults: the Amer fault example (Pyrenees, NE Spain)

M. Zarroca · R. Linares · J. Bach · C. Roqué · V. Moreno · Ll. Font · C. Baixeras

Received: 25 November 2010 / Accepted: 9 January 2012 / Published online: 24 January 2012

Abstract The combined use of geophysical and soil gas composition exploration methods allows to rapidly obtain at relative low cost information that might be related to seismic activity conditions. In this study, we carried out geochemical soil gas sampling (^{222}Rn, ^{220}Rn and CO_2), electrical resistivity tomography and seismic refraction profiles in two selected zones near the town of Amer in the Spanish Pyrenees, where the presence of recent fractures is evident in the field. Data analysis clearly reveals anomalous values for each gas at specific positions along the electrical imaging transects. Geomorphologic and hydrogeologic data and the integration of geophysical data and soil gas measurements indicate that: (1) endogene gases radon (^{222}Rn) and carbon dioxide (CO_2) are released from the meta-sedimentary basement rocks across the main fractured zones with higher permeability values, while lower Cenozoic detrital sedimentary formations act as an impervious boundary; (2) sites with highest radon concentrations (52 kBq m^{-3}) coincide with the zones in the Amer fault showing more recent geomorphic evidence of activity, and more specifically with those areas covered by thinner surficial formations; (3) the lowest ^{222}Rn values (0.2–0.4 kBq m^{-3}) were recorded just on the master active fault plane. This pattern could be explained by a dilution effect resulting from high rates of soil CO_2 efflux (267 g m^{-2} day^{-1}); (4) soil thoron (^{220}Rn) activity is maximum (143 kBq m^{-3}) in areas with high surficial fracturing; (5) groundwater pumping may cause important distortions in the natural flow dynamics and in the measured concentrations of gases. The agreement between the different data (geochemical, geophysical, and hydrogeological) and field observations (geology and geomorphology) leads us to propose a preliminary tectonic-gravitational model for the study area.

Keywords Active fault · Electrical resistivity tomography (ERT) · Seismic refraction · Soil radon and thoron activity concentration · Soil CO_2 efflux · Pyrenees · Spain

M. Zarroca (✉) · R. Linares · J. Bach
Grupo de Geodinámica Externa e Hidrogeología, Dpto. de Geología, Edificio Cc, Universitat Autònoma de Barcelona, 08193 Bellaterra, Barcelona, Spain
e-mail: mario.zarroca.hernandez@uab.cat

C. Roqué
Geodinámica Externa, Dpto. Ciencias Ambientales, Universitat de Girona, 17071 Girona, Spain

V. Moreno · Ll. Font · C. Baixeras
Grupo de Física de las Radiaciones, Dpto. de Física. Edificio Cc, Universitat Autònoma de Barcelona, 08193 Bellaterra, Barcelona, Spain

Introduction

Knowing about the degree of activity of a fault is a matter of great concern when evaluating the seismic hazard in a specific region. Stratigraphic, structural, and geomorphic studies are the usual methods that have been employed in the recognition and characterization of active faults. When combining those traditional methods with geophysical surveying techniques and gas measurements in soil and water can considerably improve the neotectonic information.

In recent years, near-surface geophysical prospecting has become a standard tool for the study of seismically active faults in a variety of geological and tectonic contexts (e.g. Vanneste et al. 2008). There is not an optimal geophysical method or technique which fits all the possible geological and environmental scenarios. Very often, the

most suitable strategy consists of the combination of different geophysical methods (e.g. Linares et al. 2010). One of the most commonly used ones is electric resistivity tomography (ERT) (e.g. Colella et al. 2004; Rizzo et al. 2004; Nguyen et al. 2007; Caputo et al. 2007). Among the main specific targets of the geoelectrical investigation of fault zones are the location and geometry of the fault planes, including blind structures, and the displacement estimation. Despite successful investigations (e.g. Zhu et al. 2009; Suski et al. 2010), the geoelectrical investigation of fault zones has not yet been globally adopted as a customary technique in studies on Quaternary tectonics or seismic hazard assessment (Fazzito et al. 2009). Particularly, in the European context, the use of ERT across fault traces or fault scarps has experienced a significant increase in the past 10 years (McCalpin 2009). ERT data comprises several advantages over other geophysical methods. Its depth of penetration is not limited by moisture, salinity or presence of clays as occurs with GPR data. Moreover, resistivity data do not encompass ambiguity related to the effect of the water table, as observed in refraction seismic data (McCalpin 2009).

An innovative, quick, and relatively cheap method to investigate active tectonic structures, using soil gas (e.g. Baubron et al. 2002) and water gas (González-Díez et al. 2009) composition in fault zones and may provide relevant information about regional stress conditions. One of the indicators considered as potential precursory to earthquakes are the changes in radon concentration linked to fault areas (Igarashi et al. 1995).

As it is known, radon is ubiquitous in the earth's crust because uranium and thorium are present in almost all rock and soil types. Actually, the ^{226}Ra isotope, upon decay, generates ^{222}Rn, known as radon (half life of about 3.823 days), whereas ^{232}Ra decaying generates ^{220}Rn, known as thoron (half life of only 55.6 s). Owing to their different half lives, ^{222}Rn and ^{220}Rn in soil/gas have different sources, i.e. from relatively deep to shallow formations for ^{222}Rn, to shallow formations for ^{220}Rn. Recent studies showed that soil ^{222}Rn concentrations tend to increase in the vicinity of the main fault planes. This behavior has been explained as a change in the rock properties associated with faults: (1) higher soil permeability to gas, (2) higher surface-to-volume ratio in the fractured rock that facilitates radon release from the solid matrix. Owing to its short half life, any radon created must be near the free surface of a rock to have any probability of escaping into the gas phase (Giammanco et al. 2009). In several cases, anomalies of soil gas ^{222}Rn and other trace gases are correlated with strong degassing of carbon dioxide (CO_2), thus substantiating a model of an advective transport of radon through the soil column by a carrier gas whose flux is controlled by pressure gradients (e.g. Toutain and Baubron 1999; Beaubien et al. 2003). Among the soil gases in volcanic or geothermal environments, CO_2 is normally the most important in terms of both abundance and efflux. For this reason, correlating ^{222}Rn and CO_2 measurements in soil gas emissions improves the assessment of the ^{222}Rn flow pattern.

Amer sector—at the southern region of the Spanish Pyrenees—was selected as the study area because of its particular regional geotectonic setting, encompassing the Amer–Brugent faults and the volcanic manifestations of the Garrotxa area. Gas-rich spring waters directly linked to Quaternary active faults are common in the studied area and around the region where it is included (Fig. 1) (Linares et al. 2001). The endogenous origin of the CO_2 present in groundwater has been demonstrated by other studies carried out in the same zone (Redondo and Yélamos 2005).

Changes in meteorological and seasonal factors can modify radon concentration in water of soils and intermittent springs (Wattananikorn et al. 1998). Recently, continuous measurement surveys carried out in the Amer area (Font et al. 2008) and in the nearby Garrotxa area (Moreno et al. 2008, 2009) show a decrease in radon and thoron during the winter season.

Taking into account the previous considerations, we carried out a geochemical and geophysical study in two selected sections across the Amer fault north of Amer town. The aim of this work is to evaluate the potentiality of the integrated application of electrical resistivity tomography (ERT) and soil radon ^{222}Rn measurements for investigating active faults.

Geological setting, neotectonics, and seismic activity

Available geological maps at 1:25,000 scale by Puig et al. (1997) provide a comprehensive knowledge about the bedrock geology of the Amer fault area.

With regard to landforms and surficial deposits, a detailed geomorphological map was elaborated on the basis of aerial photograph interpretation using black- and white aerial photographs (1957 1:33,000 scale; 1982 1:18,000 scale) and color orthophotos (2008 1:5,000 scale) and field surveys focused on tectonic landforms and Quaternary deposits (Fig. 2).

Amer area geology

The Amer fault is a late neogene NW–SE trending normal fault and is one of the westernmost structures in the fault system controlling the Empordà Neogene basin (Ferrer et al. 1999, 2001) (Fig. 1). The Amer fault is a system of parallel fault strands of about 30-km-long with planes dipping around 60° to the NE and a maximum vertical displacement that varies between 1,000 and 1,400 m (Saula et al. 1996).

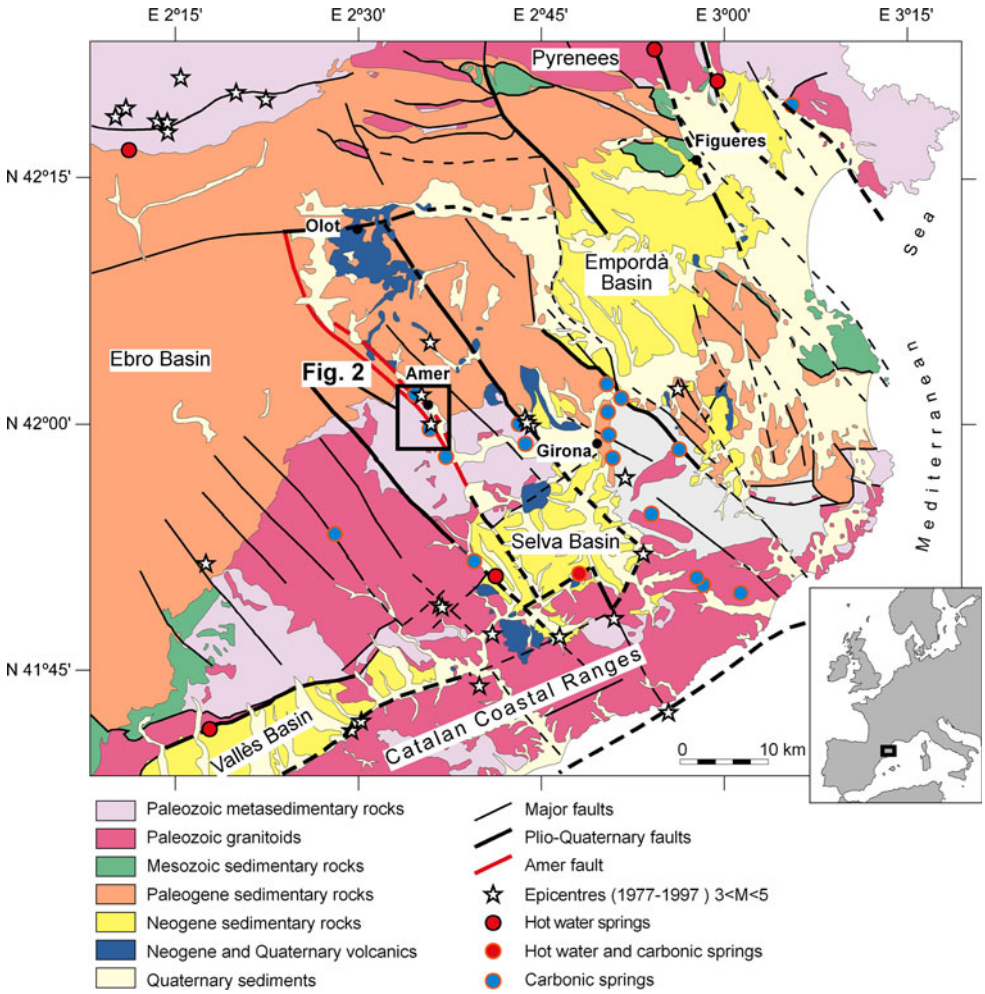

Fig. 1 Location of the studied zone in the seismotectonic context of the Eastern Pyrenees. Lithology and structural data modified after ICC (1989). Hydrothermal data from Linares et al. (2000), (2001). Seismicity data from ICC (1999)

Rocks in the surroundings of Amer town belong to the Paleozoic basement of the Catalan coastal ranges and to the Cenozoic sedimentary cover (Fig. 2). Three Paleozoic units are present in this area: (1) Cambrian–Ordovician gneisses, (2) Cambrian–Ordovician schists with intercalations of marbles and quartzites, and (3) Ordovician schists and slates with interbedded quartzites and conglomerates. Numerous dikes of igneous rocks, mostly E–W oriented and meter-sized in width, are intruded throughout the Paleozoic units. The Paleozoic basement is unconformably covered by sedimentary Cenozoic units, from Paleocene to Eocene in age: (1) continental conglomerates, sandstones and red lutites, (2) marine limestones, which form large structural surfaces and cliffs, and (3) marine marls and sandstones.

Erosion of Cenozoic sediments has exhumed a pre-Tertiary planation surfaces cut-across Paleozoic rocks. In the western side of Amer valley, this planation surface is located at an elevation of 850 to 900 m, but on the eastern side, it lies at an altitude of 250 m or less, as a consequence of the displacement on the Amer fault. This planation surface is in turn slightly tilted (<5°) to the north, probably due to the Paleogene Pyrenean orogenic compression prior to the Neogene extension.

A small volcanic outcrop exists south of Amer. It is composed by a basaltic lava flow and an eroded volcanic neck. No precise data of its age is available, but it may be chronologically and genetically related to other Quaternary volcanoes which are widespread in the Garrotxa area, some of them associated with the Amer fault.

The Brugent river, which drains the Amer valley, has developed a stepped sequence of alluvial deposits (alluvial fans and river terraces) along the valley bottom and sides (Fig. 2).

Three levels of river terraces have been identified according to their topographic position with respect to the riverbed: (1) the higher terrace (terrace 3) is located at a relative height of 30–25 m; as compared to other terraces, the greater weathering degree of the cobbles is consistent with an older age; (2) the medium terrace (terrace 2) lies between 12 and 8 m high above the current channel, and (3) the lower terrace (terrace 1) is the most extensive alluvial level and is located at a relative height of 5–3 m.

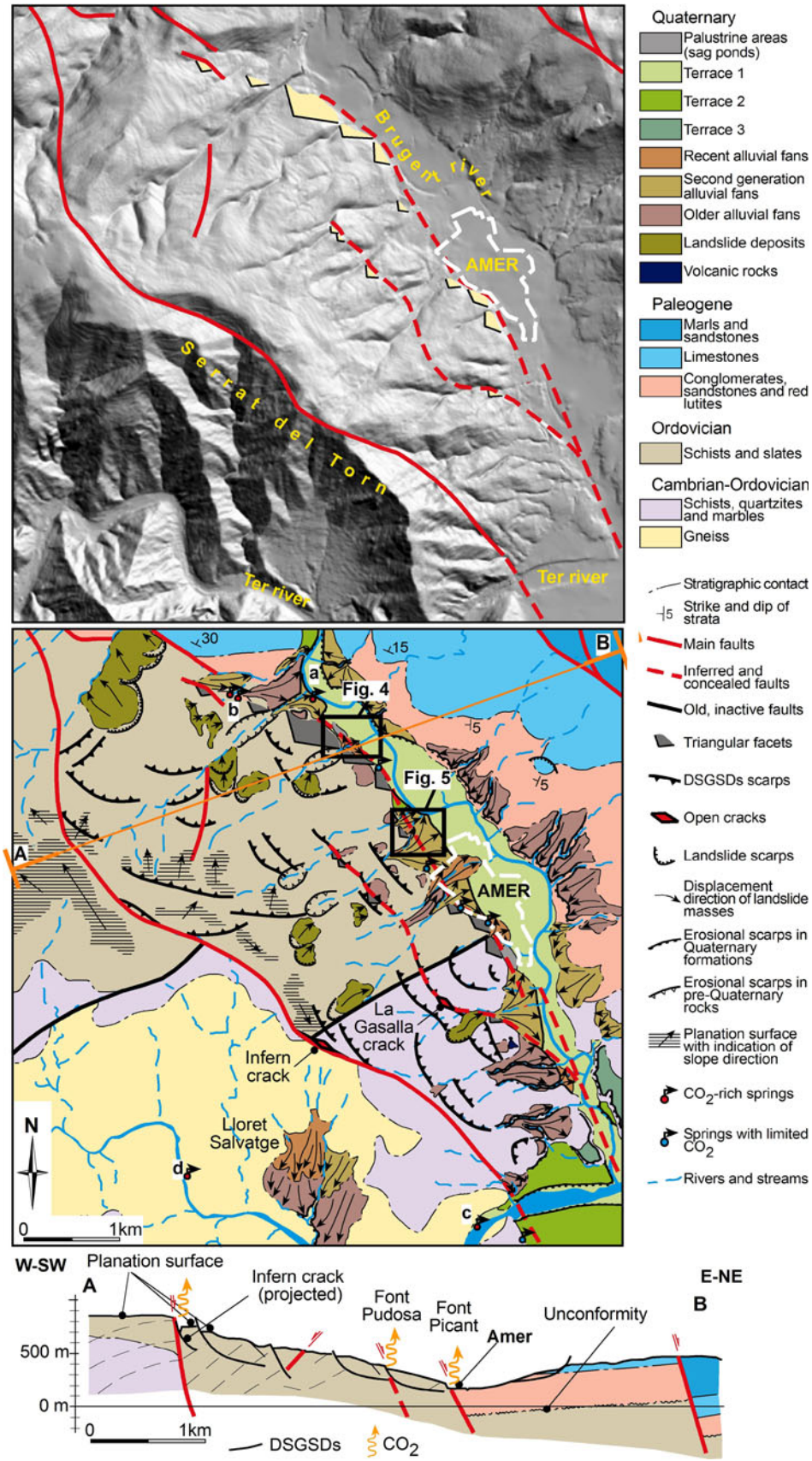

Fig. 2 Geological and geomorphological map of the Amer area. Hillshade elevation model elaborated using altitudinal data from Institut Cartogràfic de Catalunya (ICC), scale 1: 5,000. Geologic cross section modified after Puig et al. (1997). **a** Font Picant d'Amer, **b** Font Pudosa, **c** Font Picant del Pasteral, **d** Font Picant de Lloret Salvatge

Alluvial fans with their apexes upstream in the mountain front are distributed along the contact between the fluvial terraces and the rock slopes in the Amer valley. They are composed by debris-flow deposits and, sometimes, by fluvial deposits in the distal zone. According to their topographic position, geometrical relationship with fluvial terraces and degree of conservation, we have identified three generations of alluvial fans (Fig. 2): (1) the oldest alluvial fans are located at higher topographic levels and have been heavily dissected by the current streams. Most of them are associated with a fault roughly running across halfway of the mountain slope, and to the south end of the westernmost fault. (2) The alluvial fans ascribed to the second generation are eroded by the current streams and perched with respect to the river terrace 1. They are situated in the lower part of the mountain front, covering the fault line that delimits the rocky slopes. In addition, (3) the recent alluvial fan generation is barely eroded by the current streams; they are attached to the rocky slopes and overlap the second generation fans and the river terrace 1.

One of these recent fans, located very close to one of the studied profiles, has been dated by means of the ^{14}C method. Included charcoal wood fragments provided a radiocarbon age of 185 ± 30 years BP, which is consistent with historical records indicating a sporadic activity of local alluvial fans in Amer between the seventeenth and the eighteenth centuries.

Southwest of Amer, in the vicinity of Lloret Salvatge village, the deposits of the oldest alluvial fan generation are not dissected, but overlapped by the most recent ones (Fig. 2). Here, only debris-flow sediments are present. They may be considered as aggradational fans in the sense of Harvey (2002). This sequence suggests that uplift rate of the mountain would be greater than dissection rate in the Ter river.

Neotectonics and seismicity

According to Ferrer et al. (1999) and Fleta et al. (2001), two lines of evidence support a more recent tectonic activity on the Amer fault as compared to the other faults in the region: (1) migration of basaltic rift-type volcanism towards the west since Late Miocene times; the youngest lava flow (dated ca 10,000 years BP, Guérin et al. 1986) is related to the volcanoes situated along the Amer fault, and (2) morphometric analysis suggesting a very young topography controlled by the recent activity of the fault. Other geomorphologic evidence of recent includes the presence of triangular facets and meter-sized scarps developed in Quaternary alluvial fans along the fault.

Additional evidence for current activity is the historical record of damaging earthquakes in the region. During the fifteenth century, the Amer and Olot areas were affected by one of the most destructive seismic crisis ever recorded in NE Iberia. Several earthquakes that took place in 1427 and reached epicentral intensities ranging between VI and VIII have been attributed to the Amer fault (Olivera et al. 2006; Perea 2009) (Table 1). Between February and May 1427, the spatial and temporal earthquake clusters completely destroyed the towns of Olot, Amer and many others in the surrounding area. The May 15, 1427 earthquake caused at least 15 deaths in Olot.

Table 1 List of the most destructive earthquakes in the 1427 seismic crisis, attributed to the Amer fault (after Olivera et al. 2006)

Date	Intensity (EMS-98)	Magnitude (Mw)	Epicenter
May 13	VI–VII		NW Amer
May 14	VI		NW Amer
May 15	VI		NW Amer
May 19	VIII	5.9	SE Amer
May 22	VI–VII		Lloret Salvatge
May 15	VII	5.8	Olot

Regarding Amer village, despite its total destruction, historical chronicles do not mention any fatality due to collapse of buildings. However, the earthquake of April 22, 1427 with the epicenter located around Lloret Salvatge, triggered a phenomenon of gases emanation; the next day fumaroles of toxic gases through opened cracks were reported between the villages of Lloret Salvatge and Amer. These gases caused two deaths, and nine people were seriously injured. One of these cracks, called "Esquerda de l'Infern" (meaning Hell Crack in Catalan), can be seen nowadays near the fault trace (Figs. 2, 3a).

Other indicator supporting activity on the Amer fault is instrumental seismic records and the numerous gaseous groundwater emanations. Epicenters of recent, small magnitude ($3 < M < 5$) earthquakes and several springs of waters containing endogene gases form alignments associated with the fault trace (Fig. 1). One of the most outstanding discharge points in the vicinity of Amer is the Font Pudosa spring (Fig. 3b).

Radon gas emanations are either continuously or occasionally monitored at different sites in the area since 2005 (Font et al. 2008). Measured values suggest a current activity on the Amer fault. This work includes results from that investigation.

Tectonic and gravitational morphostructures in the Amer area

Tectonic morphostructures

The Amer fault system shows two major roughly parallel fault strands in the studied area (Fig. 2). The western fault is

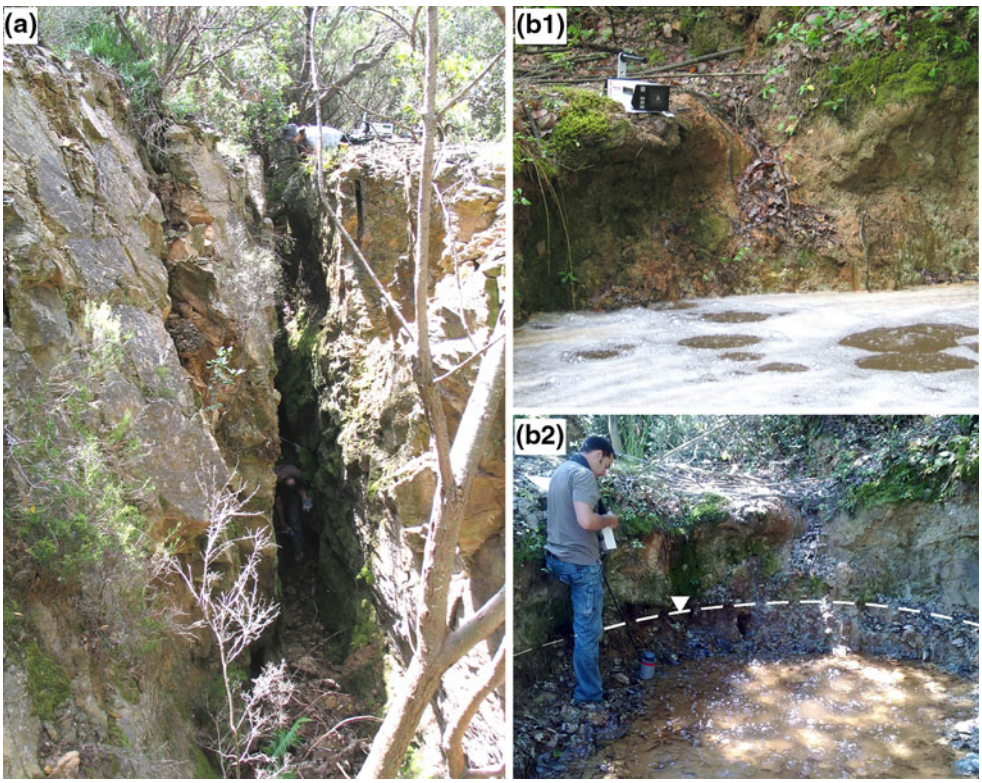

Fig. 3 **a** Esquerda de l'Infern (see person at the bottom for scale), an open crack formed by gravitational deformation of the mountain slope induced by recent coseismic activity on the Amer fault. According to historical data, this was the site where gas emanations took place during the 1427 seismic crisis. Triggered by the earthquakes, endogene gases either flowing out from the Amer fault along gravitational failure planes. Gas measurements recorded on June 17, 2010 did not show any significant anomaly. **b** Font Pudosa spring, viewed with 2 days apart. Noticeable lowering of water level. **b1** Monitoring of radon in air, May 7, 2010. Recorded value was 1,686 Bq m^{-3}. **b2** Monitoring of CO_2 air flow next to a spring water, June 22, 2010. Values reached the maximum limit for the measurement closest to the discharge site

located near the top of the Serrat del Torn mountain, relatively close to the divide between the drainage basins of Ter river and its tributary the Brugent river. Its distribution is defined by the contact between different Paleozoic units and by the displacement of the pre-Tertiary planation surface. It is recognized in the field as a shear zone with about 3 m of crushed rock. The eastern fault strand runs across the western margin of the Brugent river valley, covered by alluvial deposits of the western side. It consists of two, sometimes three, parallel fractures. In the Font Pudosa outcrops, the fault plane is composed of a 4–6 m of wide breccia.

Two geomorphologic features indicate recent activity on the eastern fault system: triangular facets and meter-sized topographic scarps. The triangular facets are distributed along the lower slopes on the right margin of Brugent river valley. Ferrer et al. (1999) and Fleta et al. (2001) identified two generations of facets, and suggested that the younger one has a Plio-Quaternary age. Oldest facets, located in the middle-lower parts of the mountain slope (Fig. 2), are strongly degraded and, in our opinion, it is difficult to establish whether they are true fault facets or landslide scars.

Meter-sized scarps occur on the surface of Quaternary deposits covering the eastern fault. Scarps interpreted as faults scarps produced by the Amer fault activity have been previously identified in the area (Ferrer et al. 1999; Fleta et al. 2001). These scarps are present where the fault trace is overlain by old alluvial fans. According to Fleta et al. (2001), no evidence of surface deformation is found in areas underlain by very recent deposits. Unfortunately, it is difficult to unequivocally identify fault scarps in this area because farming activity has been concentrated for centuries on the surface of alluvial fans and river terraces; anthropogenic scarps are abundant, and the fault scarps may have been reworked by human activity. Geophysical surveys and trenching are needed to elucidate the origin of the scarps.

Gravitational morphostructures

Landslide scarps and landslide deposits are irregularly distributed along the eastern slope of the Serrat del Torn mountain (Fig. 2). Most of them are slides that grade into

earth-flows and debris-flows downhill. In some cases, these deposits merge with alluvial fans.

Features attributable to deep-seated gravitational slope deformations (DSGSDs) are also present in the Serrat del Torn slopes. They may be classified as sackung-type (Soldati 2004). Sackung can be described as sagging of a slope due to visco-plastic deformation taking place at depth which affects high and steep slopes made up of homogeneous, jointed or stratified rock masses showing brittle behavior (Zischinsky 1969; Bisci et al. 1996). DSGSDs structures in the Serrat del Torn mountain are characterized by a set of parallel scarps and counterscarps with linear to curvilinear traces, which are distributed between the two main tectonic faults (Fig. 2).

Some open cracks associated with DSGSDs scarps have been identified. Coseismic DSGSDs (sackung-type) in the Amer area can be supported not only by the geologic and tectonic context but also by the historical chronicles. As previously explained, after or during the earthquakes of 1427, several cracks opened in the mountain and toxic gases emanated from them. The Esquerda de l'Infern crack, in the watershed between the Brugent valley and the Ter valley, lies very close to the western fault and may be directly related to the emission of gases that killed two people on April 23, 1427 (Fig. 3a). The La Gasalla crack is placed above the medium slope of the Serrat del Torn mountain, and there is no indicating that it could be related to the 1427 earthquakes. Triggering of sackung scarps by seismic shaking in the Pyrenees has been previously suggested by Gutiérrez et al. (Gutiérrez-Santolalla et al. 2005), (2008).

Geophysical surveys and soil gas test: equipment and methodology

On the basis of the geomorphological and hydrogeological indicators of recent activity associated with the Amer fault, we selected two sites to carry out the geophysical and soil gas profiles (Fig. 2). The measurement transects have been named after the places where they were acquired: Pla de la Font d'en Fàbregues profile (Fig. 4) and El Mont profile (Fig. 5). The first one was chosen because most of the CO_2-rich springs in the Amer area occur in its surroundings, whereas the second one corresponds to an area with numerous scarps on the surface of the affecting Quaternary deposits. A detailed topographic profile was done in both of them using an electronic level Sprinter 100 (Leica).

Electrical resistivity tomography and seismic refraction

The geophysical investigations consisted of electrical resistivity tomography (ERT) profiles complemented, in some areas, by seismic refraction lines (Fig. 6). These indirect data have been complemented with stratigraphical reports from wells drilling and groundwater chemical analyses from wells and springs (Table 2).

The geoelectrical data were acquired with an Lund imaging system composed by a Terrameter SAS4000 (ABEM), a 4-channel resistivimeter, and an electrode selector ES10-64e. The data acquisition was performed using a combined Wenner–Schlumberger array consisting of 64 steel electrodes with a constant spacing of 5 m, which provides a maximum exploration depth close to 55 m.

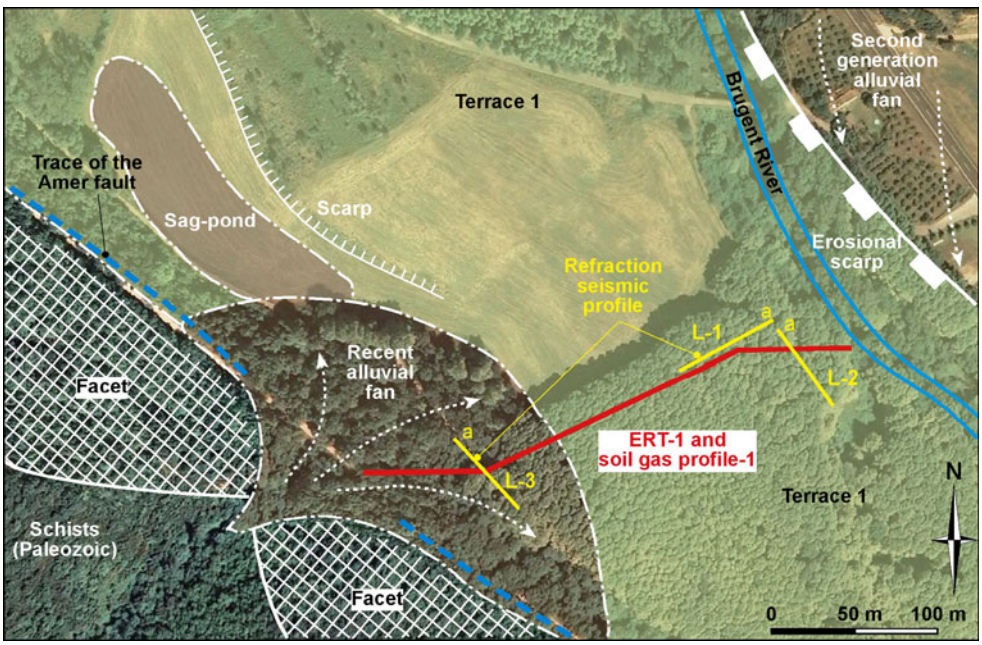

Fig. 4 Location of the geophysical and soil gas profiles in the Pla de la Font d'en Fàbregues sector (ERT-1 and soil gas profile-1). Topographic conditions do not allow crossing over the fault zone associated with the triangular facets. Seismic lines are drawn in *yellow*, with indication **a** of the direct shot point

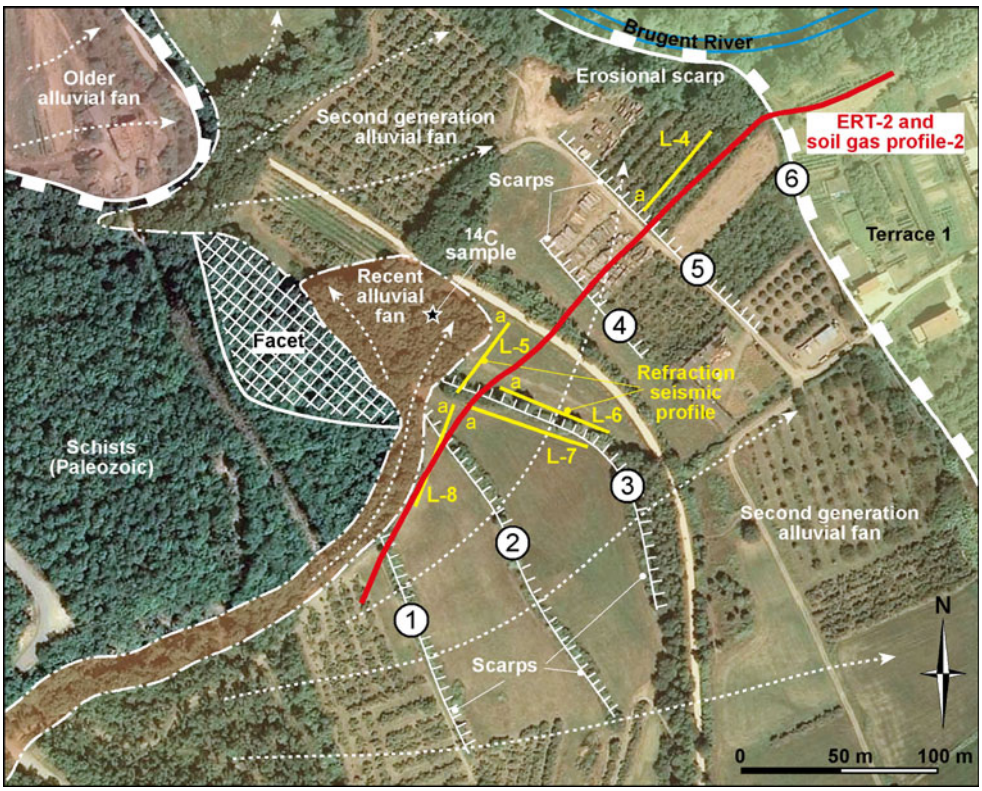

Fig. 5 Location of the geophysical and soil gas profiles in the El Mont sector (ERT-2 and soil gas profile-2). Note the presence of the numerous scarps. Geomorphological analysis allows the discrimination between those formed by tectonic events and those resulting from anthropogenic activity. *Numbers* indicate position of scarps in the corresponding ERT profile (Fig. 9). Seismic lines are drawn as in Fig. 4

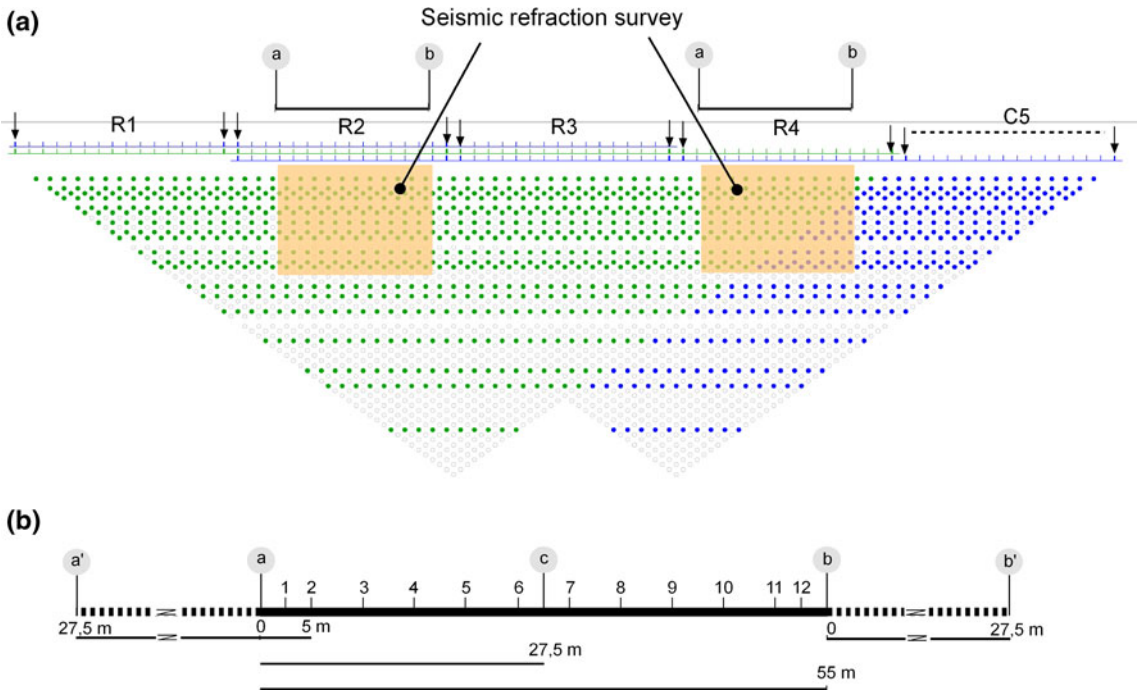

Fig. 6 Deployed geophysical arrays. **a** Electrical resistivity tomography (ERT), Wenner–Schlumberger type electrode configurations, roll along "up". This configuration consists of four aligned 16-position rolls (R1–R4) that record a total of 817 measurement points (*green*). Additional rolls (C5) add 298 new measurement points of measure (*blue*). Portion of soil involved in the seismic survey are shown as *shaded*. **b** Seismic refraction spreads. Geophone positions are plotted with numbers (*1* to *12*). *Shot points* are indicated with *letters a*, *b* and *c*

Table 2 Hydrochemical analyses from groundwater sampled in springs and wells (Fig. 2)

Code	Point type	Depth water (m bs)	Temp (°C)	EC, 25°C (μS/cm)	pH	HCO_3^- (mg/L)	CO_2 free (mg/L)	Cl^- (mg/L)	SO_4^{2-} (mg/L)	NO_3^- (mg/L)	Ca^{2+} (mg/L)	Mg^{2+} (mg/L)	Na^+ (mg/L)	K^+ (mg/L)	Fe^{2+} (mg/L)	Mn^{2+} (mg/L)
1	Spring	–	13.2	180.8	4.82	78.3	2,219.8	5.6	12.8	0.8	16	5.5	8.4	<1	<0.02	0.09
2	Spring	–	14.0	96.2	7.71	39.2	1.4	4.7	4.2	0.7	7.9	3.8	5.9	<1	<0.02	<0.02
3	Spring	–	13.5	109.2	7.36	40.6	3.3	4.2	5.3	<0.5	9.0	4.2	7.2	<1	<0.02	<0.02
4	Well	4.70	16.7	893	7.21	314.3	30.7	47	147	9.0	124	20	44	24	0.08	<0.02
5	Well	5.38	16.8	928	7.04	366.1	52.5	24.3	141	14.4	152	21	26	7.3	<0.02	<0.02
6	Spring	–	15.1	126.1	7.18	51.2	6.1	3.7	7.1	<0.5	10	3.4	12	<1	<0.02	<0.02
7	Well	3.05	16.8	1,010	7.23	279.6	25.7	38.2	151	51	154	25	28	12	0.04	<0.02
8	Well	5.55	18.2	938	6.63	296.1	107.1	43	150	14.9	136	24	34	6.4	0.18	<0.02

Collection of samples and phreatic level measurements were carried out on April 29 and 30, 2010

Measurements obtained with a Wenner array generate high potential difference readings. However, the constrains associated with its interelectrode spacing—between current and potential electrodes AM = MN = NB—imply low density of data points in the shallowest area. The combination with the Schlumberger configuration greatly improves this aspect of the array, as being less restrictive in possible electrode arrangement, thus it can generate an adequate density of points in the area nearest to the surface. The Wenner–Schlumberger array was selected for data collection, given that both horizontal and vertical geological structures and noisy urban environment were expected in the area. This method encompasses moderate resolution in both the horizontal and vertical directions, superior depth of penetration, and higher signal strength than the dipole–dipole array, resulting in a higher signal to noise ratio (Loke, 2011). On the other hand, the 2D surveying method was considered suitable for this study since the anticipated geological structures in the area are elongated and noteworthy 3D geological effects on the data were not expected.

The time history of the injected current corresponds to a box-car function of alternating polarity (3 cycles) 2 s of duration. The electrical coupling of the electrodes with the subsurface was enhanced by adding water with dissolved salt to each electrode boundary, to reduce the contact resistance between the electrodes and the ground.

The apparent electrical resistivity data are then tomographically inverted into "true" electrical resistivity distributions in the probed subsurface regions, using the RES2DINV software package. The inversion routine is based on the smoothness constrained least squares inversion implemented using a quasi-Newton optimization technique (Loke and Barker 1996). As starting model, we used constant electrical resistivity distributions equivalent to the average apparent electrical resistivity values of the corresponding pseudo-sections. The optimization method then adjusts the 2D electrical resistivity model trying to iteratively reduce the difference between the calculated and measured apparent electrical resistivity values. The root mean square (RMS) error provides a measure of this difference and thus an indication of the reliability of the final result. For the two collected profiles, convergence between the measured and the calculated data was achieved after 5 iterations with RMS errors ranging from 3.4 to 4.5%. To reduce the distortion caused by the large resistivity variations near the surface, an inversion model with a cell width of half the unit electrode spacing was used.

The distorted finite-element grid with moderate damped distortion (Loke 2000) was selected for topographic modeling. However, the Schwarz–Christoffel transformation method (Loke 2000; Spiegel et al. 1980) was used to test whether the present curvature in the field area was large enough to disturb the inverted ERT image, since the

amplitude of the curvature of the topography for the Pla de la Font d'en Fàbregues profile was similar to the depth of the deepest model layer. The results showed no significant difference between both methods.

With regard to the profile trace, the topography conditions constrained the possibility to lay out a straight line, which may condition the resistivity of the inversion model—by a slight decrease of the modeled resistivity against the real resistivity and a slight displacement of the geoelectrical model boundaries. Nevertheless, the El Mont profile was acquired by a roll along technique—the profile is composed of three superimposed segments, minimizing the deviation of the inverted model. Furthermore, field work and aerial photography interpretation allowed confirming the position of the key geoelectrical features for both profiles, Pla de la Font d'en Fàbregues and El Mont.

To complement the electrical study, seismic refraction data were collected at selected places of the sections investigated with ERT. Seismic refraction profiling is a classical geophysical technique frequently used for the study of the surficial deposits as well as for the geometry of the contacts between units (e.g. Hecht 2003; Hofmann and Schrott 2003).

Eight spreads of P-wave refraction data were acquired using a 12-channel Geometrics ES-1225 seismograph from manufacturer EG&G Geometrics, 10 Hz geophones and a sledgehammer energy source. Geophone spacing used was 5 m; except for the first and the last geophone, which was 2.5 m from the first and the last shot point, respectively. Five shot points were used with each spread. These shots are enough to resolve the properties of shallow layers. The maximum offset was limited to 55 m both by available cable length and the ability to generate significant energy through the poorly consolidated surface sediments (Fig. 6b). The seismic data were then modeled using an iterative inversion refraction analysis software package (SIPT2) in which the first solution is generated by a delay-time method, while subsequent iterations modify the solution with ray tracing (Scott 1973).

Measurement of soil gases

Taking into consideration that a standardized procedure does not exist in the literature for measuring soil gases in active tectonic zones, we followed the most usually applied methods (see synthesis in Giammanco et al. 2009; Richon et al. 2010). Up to 16 sampling stations have been studied in each of the selected profiles, which means an average density of one measurement point every 20–30 m, according to the geomorphologic context (Figs. 2, 4, 5) and scale of research. The measurements have been repeated in those points with anomalous records to validate the results.

Measurement of radon and thoron in soil

The measurement set-up to analyze radon concentration in soil gas, CRn (Bq m^{-3}), consists of an AlphaGuard PQ 2000 PRO (AG) radon monitor, a soil gas probe and an Alpha-Pump (AP) (Genitron, Germany) (Fig. 7a). The radon detector of the AlphaGuard is based on a pulse ionization chamber (alpha-spectroscopy) with an active volume of 0.56 dm^3. Soil gas was pumped through the AlphaGuard at a flow rate of 1 dm^3 min^{-1}. The pumping continued until a plastic bag (1 dm^3 volumetric capacity), placed at the outlet of AlphaGuard, was completely filled. Then, inflow and outflow valves of the detector were closed until the measurement was carried out. Radon (^{222}Rn) and thoron (^{220}Rn) activity concentrations were recorded at 1-min intervals over approximately a 15-min period. After 3 min of the initial growth ($\sim$3 half life of ^{220}Rn) concentration values became stabilized because thoron contribution was negligible and the average of these stabilized values was taken as the radon concentration in soil gas. Thoron concentration was calculated as the subtraction of radon concentration from the initial concentration peak. Point measurements were performed on May 7, 2010 along El Mont profile; June 8, 2010 along Pla de la Font d'en Fàbregues profile; June 17, 2010 in Esquerda de l'Infern; and June 22, 2010 in Font Pudosa spring.

Soil CO_2 measurements

Diffuse CO_2 effluxes were measured using the accumulation chamber method, which consists of measuring the rate of increase of the CO_2 concentration inside a cylindrical chamber opened at its bottom which is placed over the ground surface. The chamber has an internal fan to achieve an efficient gas mixing and is connected with a portable non-dispersive infrared (NDIR) spectrophotometer (PP Systems, UK, mod. EGM4) (Fig. 7b). The change in concentration during the initial measurement is proportional to the efflux of CO_2, whose values are expressed in g m^{-2} day^{-1}. This is an absolute method that does not require corrections linked to the physical characteristics of the soil. Soil CO_2 effluxes were measured on June 17, 2010 along El Mont profile and in Esquerda de l'Infern; and June 22, 2010 along Pla de la Font d'en Fàbregues profile and in Font Pudosa spring.

Results and interpretation

Geophysical survey

Geophysical results and their explanation are given in Figs. 8 and 9. The interpretation of the electrical images is based on the integration of local information generated in

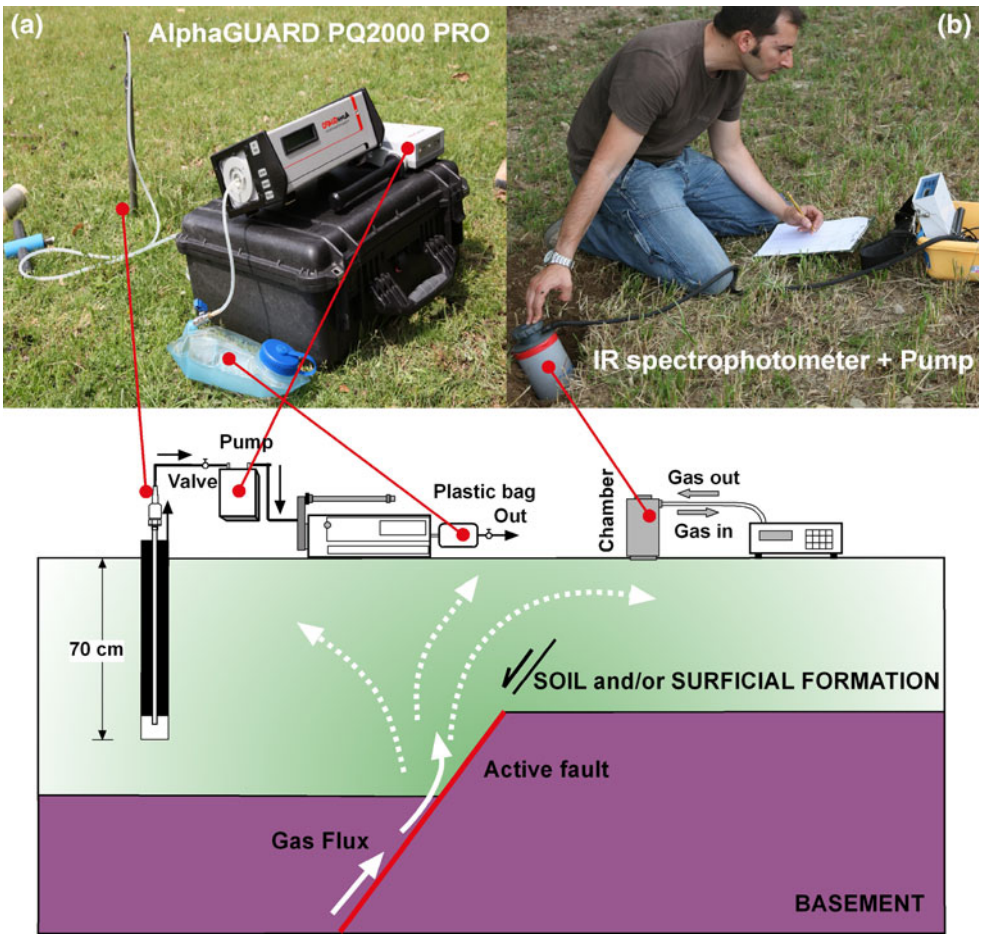

Fig. 7 Sketch illustrating the methods used in the present work for soil gas measurements. **a** Field set-up of the AlphaGuard monitor for point soil radon and thoron measurements. **b** Field set-up of the system used form recording soil CO_2 effluxes. 7a AlphaGuard PQ2000 PRO (AG) radon monitor. 7b soil gas probe and an Alpha-Pump (AP) (Genitron, Germany) and a portable non-dispersive infrared (NDIR) spectrophotometer (PP Systems, UK, mod. EGM4). One of the authors (M. Zarroca) is recording CO_2 effluxes at different depths

this study: (1) geomorphological and geological, (2) seismic and (3) hydrogeological; and general conceptual data after (4) synthetic resistivity modeling from ERT studies performed on fault models (e.g. by Louis et al. 2002) and (5) other studies carried out in areas with similarities to the Amer fault (e.g. Caputo et al. 2007; Fazzito et al. 2009; Suski et al. 2010).

Figures 8 and 9 show the most meaningful geomorphological, seismic, and hydrogeological features of the profiles. It is noteworthy that gas-containing groundwater from deep origin have a low degree of mineralization (Table 2). This is an anomalous behavior in the whole region and has been explained by a mixture of both local shallow groundwater and regional flows (Redondo and Yélamos 2000). Under the ERT geophysical point of view, this particular hydrogeologic dynamics implies variable geochemical conditions and therefore also time-variable resistivity records depending on the amount of local recharge.

Pla de la Font d'en Fàbregues profile

The main master fault in this sector is recognizable by the existence of triangular facets associated with its trace (Fig. 4). Despite being located only a few meters from the western end of the profile, it has not been possible to intersect the main fault plane (Fig. 8). Nevertheless, electrical imaging shows a westward tilting of the pre-Quaternary basement, which may be associated with the normal movement of the main fault. Antithetic oriented secondary faults fit with this explanation.

The fault splay system defining the contact between Paleozoic metasedimentary rock and Lower Cenozoic sediments plays here a secondary role. The main features related to its trace: (1) a topographic linear ridge along its surficial trace, (2) a sag-pond developed in the hanging wall, and (3) westward dipping of the electrical contact in depth, did not allow confirming whether a kinematic behavior was ascribable either to reverse or normal faulting.

A clear correlation between surface morphology and deep tectonic processes may be inferred from the profile. Surficial formations, mainly alluvial deposits up to 10–12-m thick, show a wedge-shaped geometry filling a half-graben structure.

Deep upwards groundwater flow takes place along the main fault zone. It coincides with bubbling springs in the surface. Phreatic level is shallower under the Brugent River

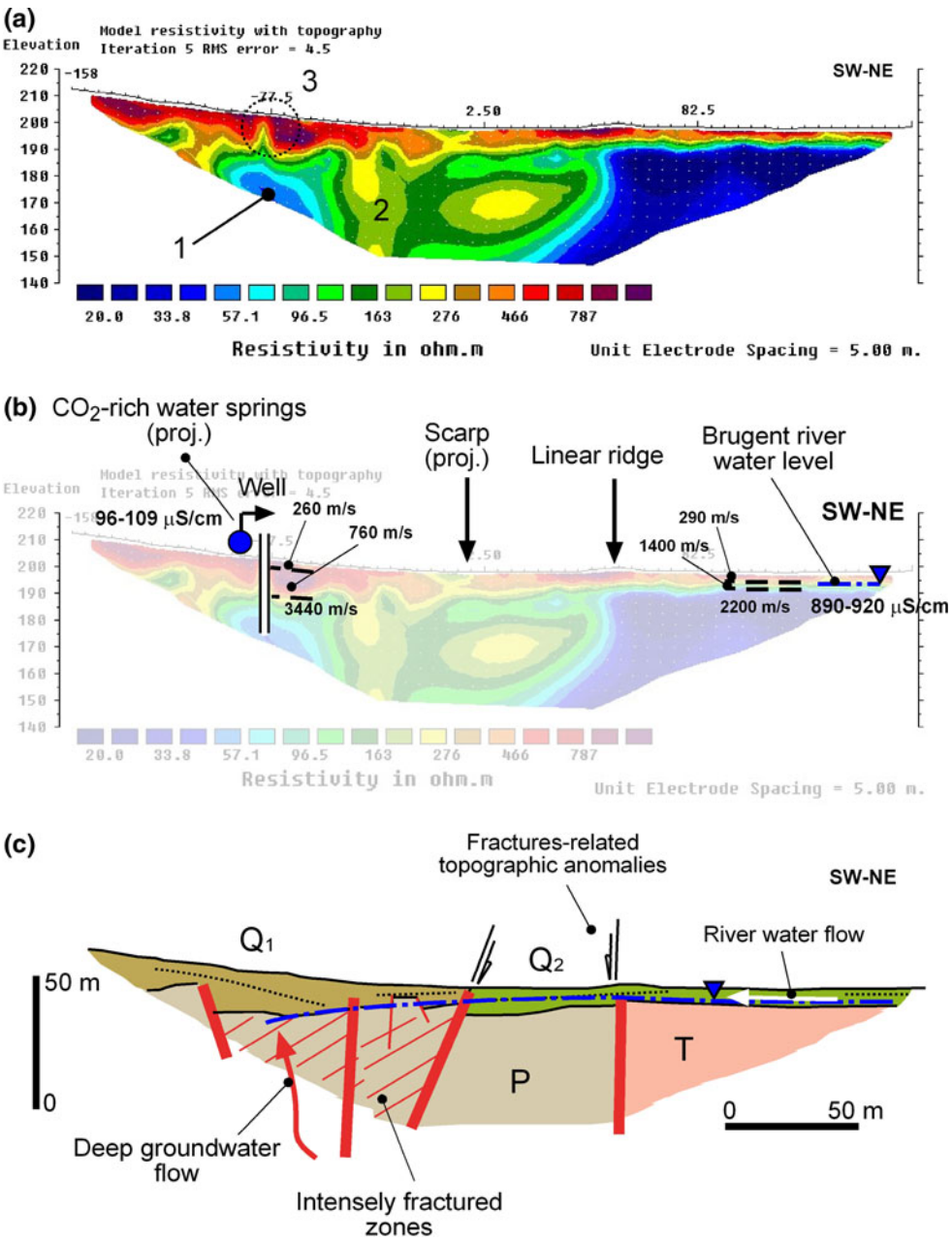

Fig. 8 Pla de la Font d'en Fàbregues general electrical resistivity profile (ERT-1, see Fig. 4 for location). **a** Resistivity profile obtained with an electrode spacing of 5 m, iteration 5 and RMS error 4.5%. *Numbers* indicate examples of electric anomalies: *1* fractured zones with groundwater flow, *2* fracture zones with limited groundwater flow, *3* well. **b** Superposition of available geology, geomorphological, and hydrogeological data along the profile (see also Figs. 2, 4). Seismic refraction results are synthesized by *dashed lines* indicating the main refractor and average velocities in m/s. Water conductivity values come from the nearby well and CO_2-rich springs. **c** Tentative interpretation of the profile showing the main geoelectric units. Basement fault zones with *inclined red lines* are areas that concentrate deep groundwater flow and/or show a strong electric heterogeneity. *Continuous lines* mark the limits between different facies and depositional units. *Dashed lines* represent the internal structure of the Quaternary deposits. *Q1* Alluvial fans, *Q2* terrace 2, *P* Paleozoic rocks, *T* Cenozoic continental sedimentary rocks. Geometry of the phreatic level, represented as *blue dashed line* with *dots*, is interpreted as a consequence of depression cones induced by pumping wells

and deeper over the fractured zone where several pumping wells exist. The water flow is directed to the west, indicating that groundwater extraction is generating a depression cone. This is supported by the resistivity profile showing a low resistivity boundary, probably depicting the water table level. The boundary departs from the top of the low resistivity layer at the NE, becoming slightly convex towards the SW and connects the low resistivity layers at the NE to the low resistivity body at x position −77.5 m. (Fig. 8a).

Seismic refraction surveying allowed defining three main seismic layers: (1) an upper layer, continuous along the entire profile, characterized by seismic velocities of 260–290 m/s and corresponding to the uppermost parts of colluvial/alluvial deposits highly disturbed by human activity; (2) an intermediate layer, located at the SW sector, with a seismic velocity of about 760 m/s corresponding to colluvial deposits probably underlain by highly altered bedrock; (3) and a lower layer presenting a seismic velocity of about 3,500 m/s at the SW sector and of 2,200 m/s at the NE sector, both corresponding to bedrock interpreted as schists at the SW and lutites and sandstones at the NE. A refractor characterized by seismic velocity of 1,400 m/s, between the upper and the lower seismic layers may be interpreted either, as water table refraction or as the weathered uppermost sections of the lutites and sandstone bedrock.

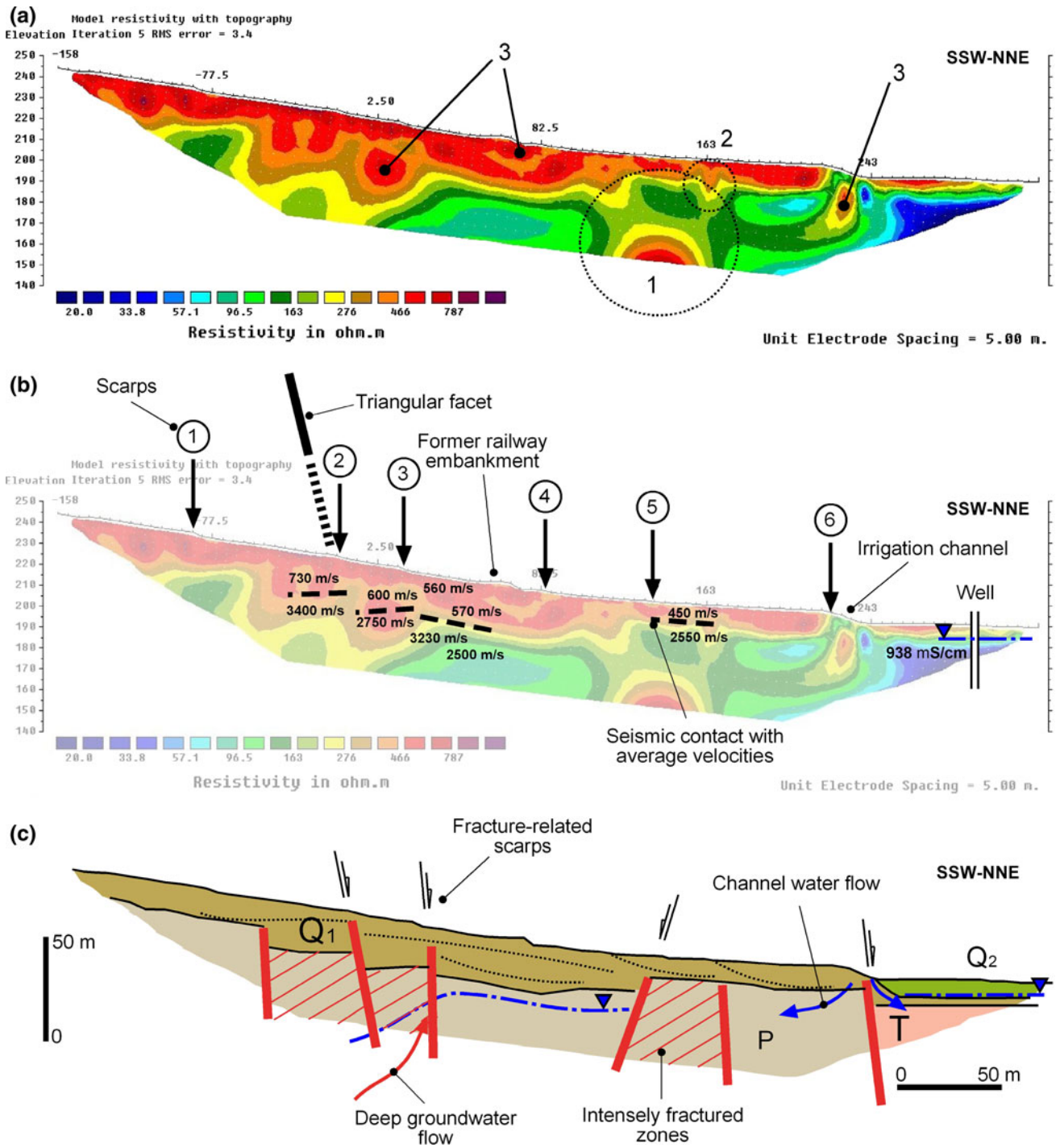

Fig. 9 El Mont general electrical resistivity profile (ERT-2, see Fig. 5 for location). **a** Resistivity profile obtained with an electrode spacing of 5 m, iteration 5 and RMS error of 3.4%. *Numbers* indicate examples of electric anomalies: *1* fractured zones, *2* open cracks, *3* fault scarps. **b** Superposition of available geology, geomorphological, and hydrogeological data on the profile (see also Figs. 2, 5). Seismic refraction results are synthesized by *dashed lines* indicating the main refractor and average velocities in m/s. Water conductivity value correspond to the well. **c** Tentative interpretation of the profile showing the main geoelectric units. Basement fault zones with *inclined red lines* are areas that concentrate deep groundwater flow and/or show a strong electric heterogeneity. *Continuous lines* mark the limits between different facies and depositional units. *Dashed lines* represent the internal structure of the Quaternary deposits. *Q1* Alluvial fans, *Q2* terrace 2, *P* Paleozoic rocks, *T* Cenozoic continental sedimentary rocks. Only scarps numbered as *2*, *3*, *5* and *6* match with offsets at depth

El Mont profile

Recent tectonic deformations are also present along this profile. Like in the Pla de la Font d'en Fàbregues profile, the main fault affects metasedimentary Paleozoic rocks. The profile reveals a depressed, half-graben-like area close to the fault plane, which is filled with Quaternary sediments. Some antithetic secondary faults may also be traced (Fig. 9). Electrical imaging allows the differentiation between tectonic scarps and those of anthropogenic origin (Fig. 5). Quaternary deposits reach up to 22 m in thickness, suggesting a higher subsidence rate here than in the Pla de la Font d'en Fàbregues profile. Regarding the groundwater flow pattern, the resistivity data shows greater uncertainty than the Pla de la Font d'en Fàbregues profile. On the other hand, well drilling register is only available in the NNE region. Nevertheless, electrical imaging suggests that groundwater levels are irregular and do not show continuity from the eastern to the western parts of the profile. Water table within Quaternary sediments is only detected under the Brugent river alluvial sediments.

The seismic refraction model was simplified to two main seismic layers: (1) an upper layer with velocities between 450 and 730 m/s corresponding to colluvial deposits; (2) and a lower layer with velocities between 2,500 and 3,400 m/s, corresponding to bedrock—schists.

Soil gas

Coordinates of soil gas sampling points, dates of measurement and the results are shown in Table 3.

Pla de la Font d'en Fàbregues profile

Distribution of radon ^{222}Rn and thoron ^{220}Rn concentration in soil, and CO_2 efflux along the transect are given in Fig. 10a.

Soil radon concentration in the area has been explored with the Clipperton probes and LR115 radon detectors by previous studies (Font et al. 2008). The variability of the results showed a very clear seasonal effect on soil radon levels, which can be up to 14 times higher in summer than in winter. Our values, obtained with an AlphaGuard monitor, follow a similar pattern, being in the range of 0.4–31.5 kBq m^{-3}.

According to the distribution of soil radon values, the most tectonically active segment of the profile would be the central one, but this does not coincide with the position of the main fault and its related triangular facet. Furthermore, radon values around the main fault are very low in comparison.

Soil CO_2 efflux data are also characterized by a strong variability along the profile, with a range of 27–267 g m^{-2} day^{-1} (standard deviation $\sigma = 70$ g m^{-2} day^{-1}). Highest values are recorded in the central part of the profile. There is not an obvious and specific spatial correlation between soil radon content and CO_2 efflux and such an irregular behavior could be caused by both, gas dispersing in the highly permeable soil overlying the faults and water removal in the nearby groundwater wells; nevertheless, despite the gas dispersing effect and the distortions due to local water extraction, value ranges are considerably high for both radon and CO_2, which suggests that endogene gases outflow through deep fractures.

Thoron presents a similar trend to radon in the profile. It must be noted that the lowest thoron value is recorded near to one of the pumping wells located very close to the transect line. When considering a shallower origin for thoron, coming out from near-surface fractured zones, well pumping is a coherent explanation for such a low value.

The systematic measurements taken alongside the profile have been complemented with scattered records in the surroundings of the Font Pudosa spring (Figs. 2, 3b). High values are obtained. Both radon and thoron activity concentrations are of the order of 50 kBq m^{-3}; a maximum value of 140 kBq m^{-3} has been detected for thoron. With respect to CO_2 efflux, an extreme variability between 15 and 89 g m^{-2} day^{-1} and the instrumental top of >2,400 g m^{-2} day^{-1} has been recognized within distances <5 m.

As a whole, collected data are scarce, but denote a certain trend. Highest CO_2 efflux values are present in the vicinity of natural gaseous water springs and in association with the main fault, whereas radon and thoron decrease in these same areas.

El Mont profile

Distribution of radon ^{222}Rn and thoron ^{220}Rn concentration in soil, and CO_2 efflux along the profile are given in Fig. 10b. Differing from the previous profile, soil gases in El Mont profile have a different behavior. Here, without anthropogenic disturbances due to groundwater pumping, radon, thoron and CO_2 show less pronounced temporal variability.

It is specially interesting the inverse relation detected between radon and CO_2 efflux. All along the profile, the higher the radon content (45.5–51.4 kBq m^{-3}) in a measurement point, the lower the CO_2 efflux (10.8–15.2 g m^{-2} day^{-1}). On the contrary, coinciding with the location for the main fault a negative anomaly of radon between 0.2 and 0.4 kBq m^{-3} (2.5 σ under background value) and maximum CO_2 values (201.1–226.3 g m^{-2} day^{-1}) are detected.

This close inverse correlation between radon and CO_2 efflux has already been observed in the Mount Etna, Sicilly volcanic-tectonic environment (Giammanco et al. 2009).

Table 3 Point measurement records for soil gases and sampling environment conditions

Site id	St.Nr.	Location 31T UTM		Sampling[a]		Soil[b]		^{222}Rn[c]		^{220}Rn[c]		Environment[d]			CO_2[e]	
		North	East	Date (2010)	Depth (m)	Sat. Deg. (%)	T. (°C)	C_{Rn} (kBqm^{-3})	Uncert. (kBqm^{-3})	C_{Rn} (kBqm^{-3})	Uncert. (kBqm^{-3})	Hum (%)	T. (°C)	Pre. (mbar)	Efflux (g m^{-2} day^{-1})	Desv. Stand. (g m^{-2} day^{-1})
Profile of Font d'en Fàbregues	1	4652481	465888	June 8	0.7	97	15.9	0.404	0.094	8.6	2.4	64	23	981	83.8	7.0
	2	4652479	465886	June 8	0.7	94	17.2	0.51	0.13	9.6	2.8	63	24	980	93.4	2.1
	3	4652472	465906	June 8	0.7	96	16.3	8.14	0.63	17.1	3.6	58	25	981	40.5	2.1
	4	4652465	465926	June 8	0.7	98	16.1	9.24	0.83	21.6	3.7	59	25	981	110.5	3.6
	5	4652458	465946	June 8	0.7	100	16.1	15.23	0.59	1.7	3.5	64	26	981	56.6	1.6
	6	4652457	465958	June 8	0.7	100	15.9	13.41	0.86	18.5	3.4	67	26	981	39.9	1.7
	7	4652467	465976	June 8	0.7	92	15.9	29.66	0.92	16.2	2.0	66	26	982	240	17
	8	4652476	465995	June 8	0.7	91	16.4	30.16	0.82	21.6	2.2	69	27	983	76.5	4.1
	9	4652486	466014	June 8	0.7	98	16.4	31.50	0.77	27.9	2.2	65	28	983	266.7	9.8
	10	4652496	466032	June 8	0.7	90	17.5	19.7	1.1	19.0	3.5	63	29	983	56.1	1.6
	11	4652505	466051	June 8	0.7	90	17.3	12.84	0.81	7.9	3.6	64	29	984	32.2	1.8
	12	4652515	466070	June 8	0.7	98	16.9	27.7	1.1	8.1	3.7	66	25	984	27.9	1.5
	13	4652524	466088	June 8	0.7	97	17.7	11.00	0.41	9.2	3.2	68	25	984	123.5	4.9
	14	4652530	466110	June 8	0.7	91	16.9	19.51	0.48	6.2	3.4	72	25	985	26.82	0.51
	15	4652530	466131	June 8	0.7	97	17.1	11.75	0.65	9.1	3.1	65	25	985	70.4	1.0
	16	4652531	466152	June 8	0.7	98	18.7	10.86	0.24	17.3	3.6	60	25	985	57.89	0.94
	17	4652531	466173	June 8	0.7	92	17.1	3.32	0.14	7.4	1.8	58	25	985	31.4	1.2
Profile of Mont	1	4651588	466387	May 7	0.7	87	17.5	37.09	0.98	10.5	2.8	60	23	979	78.7	3.0
	2	4651615	466419	May 7	0.7	84	18.2	31.93	0.91	12.9	3.0	62	24	979	35.1	1.7
	3	4651632	466441	May 7	0.7	88	17.6	29.3	1.3	12.7	3.0	58	24	980	54.2	1.2
	4	4651669	466457	May 7	0.7	79	17.8	22.3	1.3	9.3	3.4	60	23	980	37.6	3.7
	5	4651704	466466	May 7	0.7	84	17.7	0.40	0.10	4.7	2.3	60	22	980	181.4	3.7
	5bis	4651704	466461	May 7	0.7	75	16.4	0.2053	0.0062	4.3	1.8	65	22	979	201.1	6.3
	6	4651710	466467	May 7	0.7	80	17.0	18.09	0.51	2.9	3.1	63	23	980	226	18
	7	4651725	466475	May 7	0.7	90	17.2	33.3	1.3	4.4	3.1	–	–	–	–	–
	9	4651743	466491	May 7	0.7	75	16.4	38.9	1.3	0.0	3.5	62	21	980	80.3	3.8
	10	4651764	466535	May 7	0.7	79	17.0	38.1	1.4	9.3	2.3	55	21	980	25.2	1.7
	11	4651752	466521	May 7	0.7	76	16.7	45.4	1.8	8.9	2.8	58	22	980	10.83	0.42
	12	4651786	466557	May 7	0.7	78	16.2	51.4	2.3	9.3	3.3	54	21	981	15.25	0.67
	13	4651798	466564	May 7	0.7	81	16.5	45.0	1.6	7.4	2.6	54	20	981	10.89	0.63

Table 3 continued

Site id	St.Nr.	Location 31T UTM		Sampling[a]		Soil[b]		^{222}Rn[c]		^{220}Rn[c]		Environment[d]			CO_2[e]	
		North	East	Date (2010)	Depth (m)	Sat. Deg. (%)	T. (°C)	C_{Rn} (kBqm^{-3})	Uncert. (kBqm^{-3})	C_{Rn} (kBqm^{-3})	Uncert. (kBqm^{-3})	Hum (%)	T. (°C)	Pre. (mbar)	Efflux (g m^{-2} day^{-1})	Desv. Stand. (g m^{-2} day^{-1})
	14	4651819	466579	May 7	0.7	86	16.0	41.7	1.4	2.8	2.4	56	22	981	31.7	1.4
	15	4651843	466602	May 7	0.7	88	15.9	39.9	1.8	18.3	2.9	68	22	981	29.48	0.57
	16	4651863	466620	May 7	0.7	87	16.8	17.80	0.90	18.8	2.4	65	21	982	70.4	6.9
	17	4651886	466682	May 7	0.7	90	16.4	17.29	0.54	19.1	2.1	65	21	982	89.18	0.82
Font Pudosa	2	4652862	464952	June 22	0.5	96	17.4	50.2	1.7	143.4	6.5	52	22	979	69.8	1.5
	3	4652863	464952	June 22	0.5	85	17.5	53.7	2.3	51.2	4.3	53	24	980	65.9	1.8
Esquerda de l'Infern	1	4649916	465668	June 17	0.5	83	10.4	1.689	0.070	0.39	0.70	61	16	932	36.0	2.4

The error is quantified as the standard deviation

[a] Date of sampling and depth of borehole

[b] Temperature and water saturation degree of soil inside the borehole

[c] ^{222} Rn column: activity concentration (CRn) of ^{222}Rn calculated as arithmetic mean of point measurement series (obtained 3 min after CRn peak). ^{220}Rn column: CRn of ^{220}Rn, calculated as the difference between CRn peak and calculated CRn for ^{222}Rn

[d] Environment conditions during CO_2 sampling (air temperature, relative humidity, and atmospheric pressure)

[e] CO_2 efflux calculated as the arithmetic mean of a set of values measured during 120 s at 4.8 s intervals

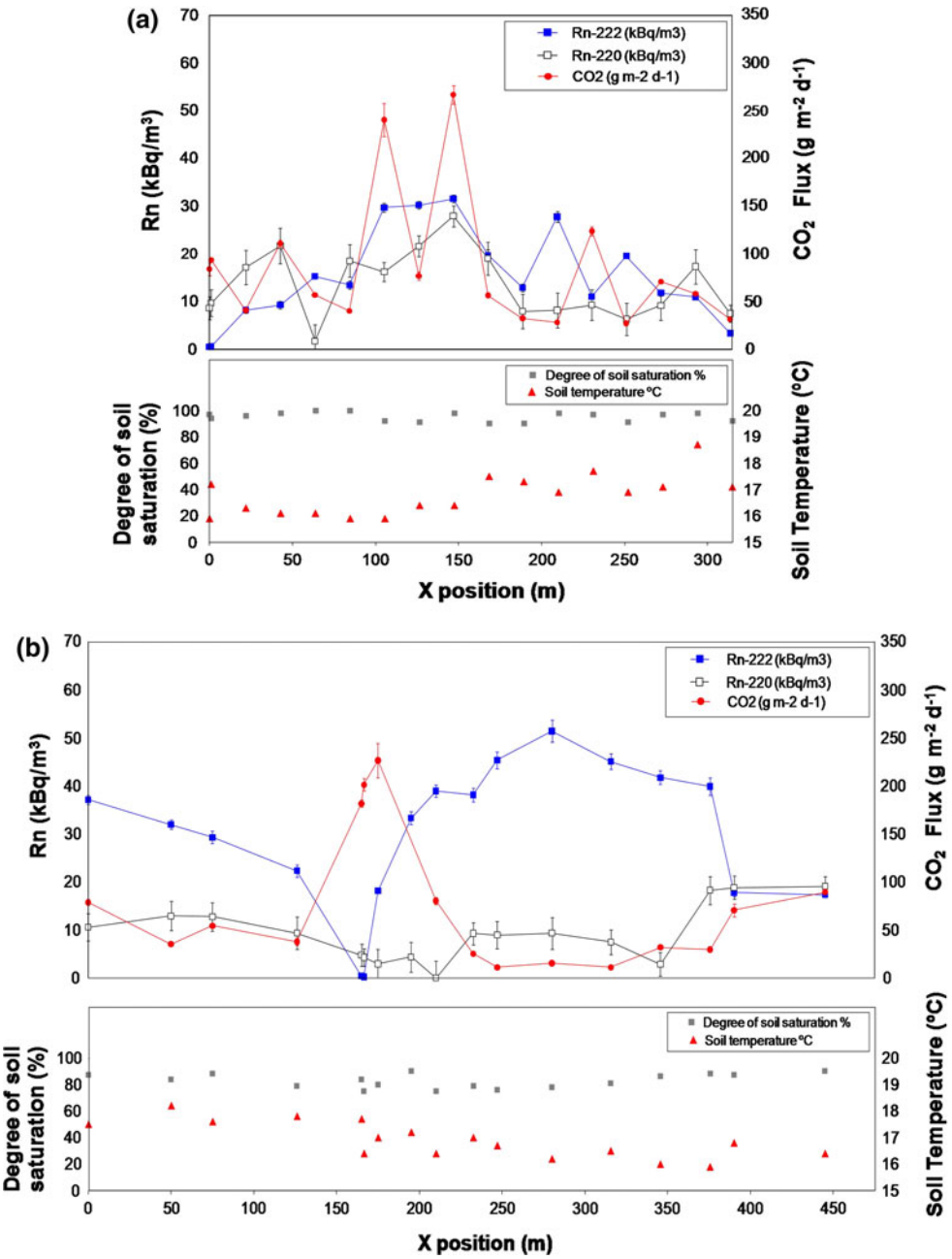

Fig. 10 Soil gas radon, thoron and CO_2 versus distance along survey lines coinciding with the two ERT profiles (*upper plots*). *Lower plots* show the degree of saturation in soil and temperature inside the hole where Rn measures were taken. The *X*-coordinate value starts in the western end of both profiles. **a** Concentration of ^{222}Rn and ^{220}Rn against CO_2 efflux in Pla de la Font d'en Fàbregues survey line (ERT-1). A negative anomaly in ^{222}Rn concentration is seen in the first measure points, and a positive anomaly in ^{222}Rn and CO_2 exists between 105 and 150 m along the profile. **b** Concentration of ^{222}Rn and ^{220}Rn against CO_2 efflux in El Mont survey line (ERT-2). A pronounced negative (^{222}Rn) and positive (CO_2) anomaly is present at 165 m in the X-position. There is also a positive anomaly in ^{222}Rn between 250 and 350 m

This pattern could be explained as a radon dilution effect resulting from high rates of soil CO_2 efflux.

With the aim to confirm the high CO_2 efflux values detected close to the scarp related to the main fault, up to 18 regularly scattered additional measurements were taken around the area. The highest values (201.1–226.3 g m^{-2} day^{-1}) are observed on both sides of the scarp, and the values progressively decrease with the distance to it. On the other hand, in the central part, where colluvial materials derived from the erosion of fault scarp are present, lowest values are measured (42.5 g m^{-2} day^{-1}).

Thoron concentrations are higher (19.1 kBq m^{-3}) in the sampling points at the eastern side of the profile, where radon values are lowest (17.3–17.8 kBq m^{-3}); meanwhile, they are around 10 kBq m^{-3} in the rest of the transect line. Several reasons may explain this behavior: lithological or textural changes in the basement or the surficial cover; variations in the hydrologic conditions; different types of faults with variable depth.

Integrated analysis

Integration of electric imaging and soil gas data allows proposing a neotectonic interpretation (Fig. 11). Several facts must be remarked.

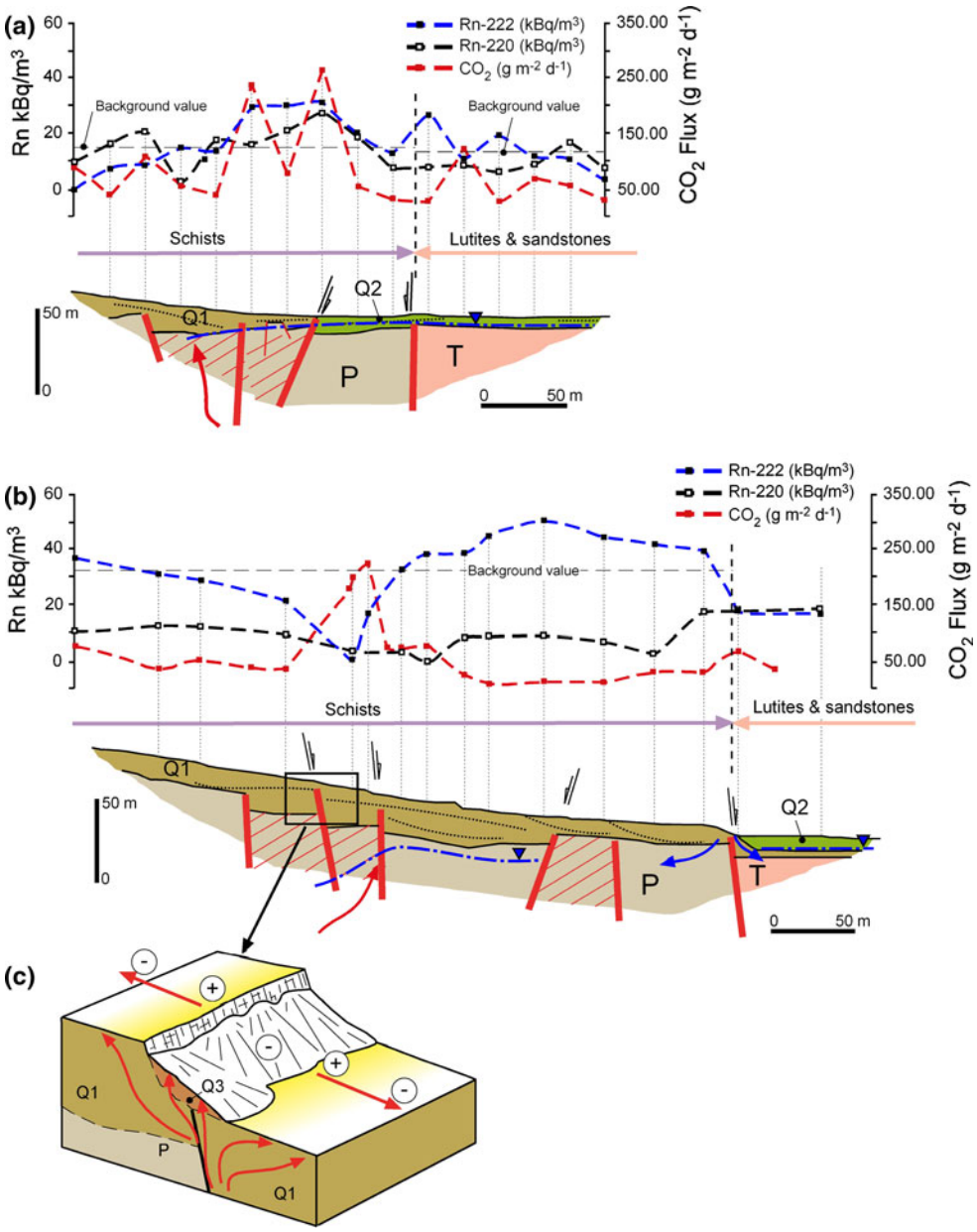

Fig. 11 Integrated geophysics and soil gas profiles. **a** Pla de la Font d'en Fàbregues profile. Radon background values have been calculated for each of the lithological domains recognized from the geophysical transect: 15 kBq m^{-3} (σ = 11 kBq m^{-3}) for the Paleozoic schists, and 14.4 kBq m^{-3} (σ = 8.4 kBq m^{-3}) for the Paleogene lutites and sandstones. **b** El Mont profile. Radon background value is 34 kBq m^3 (σ = 13 kBq m^{-3}) for the Paleozoic schists. **c** Schematic diagram depicting CO_2 efflux distribution along the indicated *scarp*. On the surface, the highest values (+), reaching up to 226 g m^{-2} day^{-1}, were recorded on the *darker shaded area*. Lowest values correspond to the *lighter shaded areas*, with records of 42.5 g m^{-2} day^{-1}. *Arrows* indicate decrease direction of the CO_2 efflux

The subsoil in both profiles is characterized by a similar distribution of materials and structures. In spite of that soil gases behave differently in the two studied transects. Erratic distribution of concentration and flow values in the Pla de la Font d'en Fàbregues profile seems to be strongly influenced by a complex hydrogeologic context. Deep and surficial fluxes meet in this area (Figs. 8c, 11a) under hydrodynamic conditions altered by local groundwater well pumping. The flow of gases coming out through a highly permeable medium is heavily modified by anthropogenic disturbances that lead to irregularities in gas concentration along the profile. The Ostwald coefficient accounts for gas solubility in water and is defined as the ratio of gas concentration in the water phase to that in the gaseous phase. The value for Ostwald's coefficient corresponding to water temperatures of 17–18°C is about 0.28 for radon gas and about 1 for CO_2 (Wilhelm et al. 1977; Clever 1985). So, under atmospheric pressure, air has the same concentration of CO_2 than water, but about four times higher radon concentration than water. Regardless of the anthropogenic effect, an excellent spatial correlation between the main fault zones and endogene gases (^{222}Rn, CO_2) anomalies is observed.

Radon distribution fits well with the principal geomorphological indicators of recent tectonic activity. Highest and lowest concentrations are found in the area with a more accumulative tectonic subsidence amount (i.e. see graben in the central part of El Mont profile, Fig. 11b). Negative

radon anomalies linked to a dilution effect by CO_2 (Giammanco et al. 2009) are specially common in such a regional context where CO_2 rich-springs and active faults are present (Fig. 1). In other geologic contexts where no CO_2 emanations exist, negative radon anomalies above active faults may be explained by the presence of impermeable clay gauge fillings (Seminsky and Bobrov 2009).

At a detailed scale, it is noteworthy to remark the particular zoned CO_2 efflux distribution related to tectonic scarps (Fig. 11c). Consistently to geophysical and geomorphological dataset, the lowest CO_2 recorded values just on the main fault trace are explained by the higher O_2 content in the colluvial materials that cover it; CO_2 is quickly released in the presence of atmospheric O_2.

The obtained results indicate that permeability and aeration degree of surficial formations that cover active fault zones play an important role in the release of endogen gases from the ground. From a methodological point of view this consideration must be taken into account for future CO_2 flow surveys carried out with surface equipment similar to that used in this study.

The inverse correlation between ^{222}Rn and CO_2 has been also explained as an instrumental artifact in previously published works (Tuccimei and Soligo 2008). Nevertheless, the experimental procedure in this other study corresponds to a soil radon flux measurement by means of a RAD7 monitor. The physical principle of radon detection differs between the RAD7 (solid state detector) and the AlphaGuard (ionization chamber). The cluster charge neutralization effect that CO_2 could produce inside the detection chamber of RAD7 influences the detection process, while this effect inside the ionization chamber of an AlphaGuard is not influential for detection. Hence, in our case, the inverse correlation observed is not considered to be instrumental.

The high radon and thoron values measured in the area of Font Pudosa spring (concentrations of radon ^{222}Rn around 50 kBq m^{-3} and thoron ^{220}Rn between 50 and 140 kBq m^{-3}) might be due, almost partially, to the existence of shallow intensely fractured materials related to gravitational phenomena (sackung-type). Purtscheller et al. (1995) suggested that large landslides may act as radon source structures since they provide, regardless the U and Ra content of the rocks: (1) numerous active surfaces, by rock fracture, favoring ^{222}Rn migration to air, (2) flow circulation pathways for ^{222}Rn-enriched air due to an increase in permeability of the landslide body.

Discussion and conclusions

Evidence of recent tectonic activity is common in areas with active faults. Their study is an important starting point for the identification of the most active fault segments, in order to select optimal locations for the excavation of trenches to infer their seismogenic potential.

In this study, the geophysical prospection campaign has lead to a better knowledge of: (1) local lithology and structure of the Amer fault zone, in particular the identification of secondary antithetic and synthetic faults; (2) geometry and internal structure of the cover Quaternary; and (3) the hydrogeological conditions, such as the position of the water table and the groundwater flow paths, despite the uncertainty posed by the limited hydrogeological data available.

Information coming from the soil gases measurement profiles has allowed us to know: (1) the amount of endogene gases (^{222}Rn, ^{220}Rn, CO_2) emanations in different segments of the fault; (2) the distribution of anomalies—relative maximum and minimum values—in each of the studied profiles; and (3) the physical interferences between ^{222}Rn and CO_2 emissions.

Apart from the aforementioned data, additional hypothesis may be stated regarding to the seismic analysis of the Amer fault. By an integration of the whole data it has been possible to get a better knowledge of (1) the fractures that facilitate migration of the endogene gases and therefore, to discriminate those of most seismic activity; and (2) the flow of gases across Quaternary deposits covering the fault zone. By integrating local geology and geomorphology, it is possible to propose new conceptual models (Fig. 12) which may lead to further advanced investigations in the region.

In synthesis, the most outstanding aspects of the proposed model for the Amer fault in the studied area are:

1. Advective transport of deep gases (^{222}Rn and CO_2) along the main fault plane occurs due to the high ground fracturation degree and permeability.
2. Concentration of ^{222}Rn and ^{220}Rn, and CO_2 efflux near the surface are influenced by the interaction of endogene gases with the existing materials and local hydrogeological and gravitational processes. It is particularly noteworthy that:
   - Dilution of ^{222}Rn by CO_2 prevails in the main fractured zones, thus producing very low radon values. The highest radon levels coincide with points of lowest CO_2 flux rate.
   - The maximum ^{220}Rn values are recorded in intensely fractured areas affected by large landslides (DSGSDs), which is coherent with the presence of shallow fractures.
   - Sedimentary formations from lower Cenozoic age act as an impervious barrier, since they are slightly fractured and include pelitic levels. That favors concentration of gases flow mainly across the metasedimentary basement.

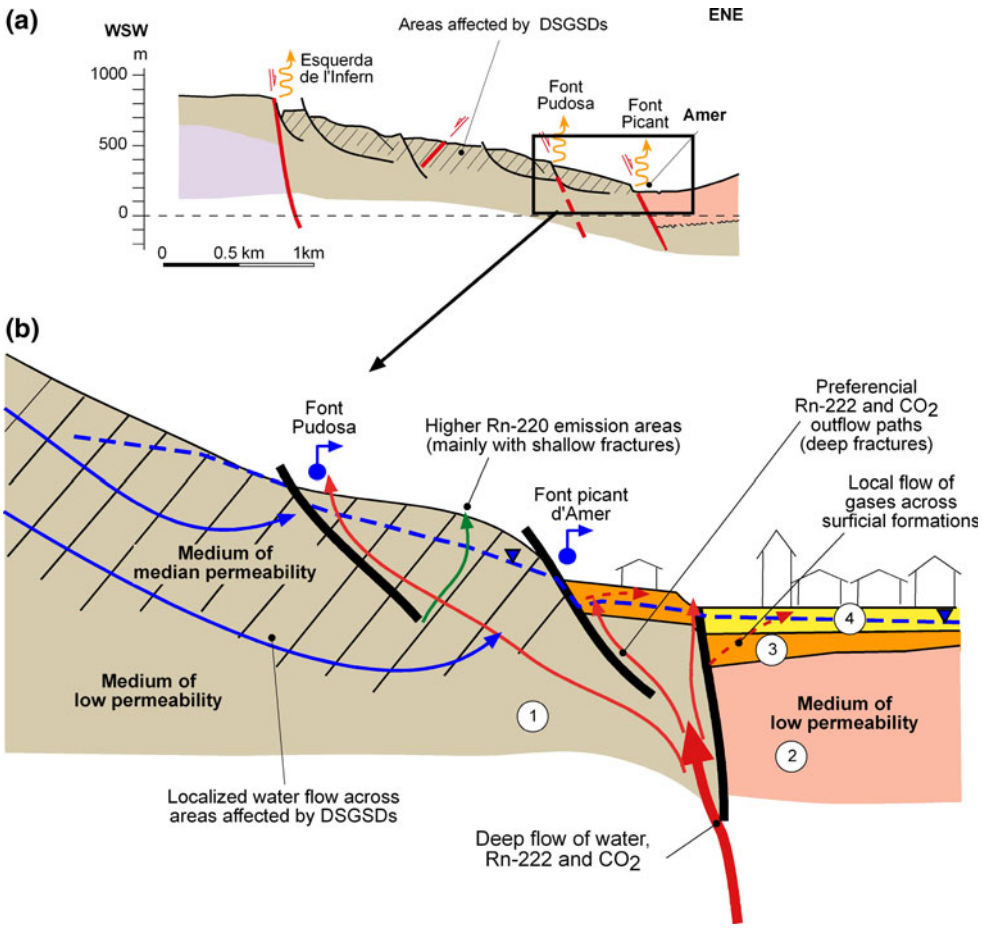

Fig. 12 Conceptual model for the outflow of endogenous gases from the Amer fault near the town of Amer. **a** Selected portion of the cross section in Fig. 2. Deep-seated gravitational slope deformations (DSGSDs, sackung-type) are believed to have formed coseismically in relation with the activity on the Amer fault trace. **b** Detailed sketch of the lower segment in the general cross section. *1* Paleozoic metasedimentary rocks, *2* Cenozoic sedimentary rocks, *3* alluvial fans, and *4* river terraces

- Quaternary formations (alluvial fans and fluvial deposits) redistribute gases around the main faults. The presence of groundwater in these formations limits substantially the exhalation of gases due to their solubility in water.

The proposed interpretation, concerning the association of higher tectonic activity on faults with higher concentrations in endogenous gases, is an attractive hypothesis notwithstanding further testing is required to assess it. Several uncertainties over the relationship of endogenous gases with tectonic activity still remain. The simultaneous use of geophysical prospection techniques and soil gases profiles provide with valuable information, especially in areas where features related to recent surface deformation are obliterated. Uncertainties derived from the use of a specific technique are minimized or even removed when several methods are combined. Taking into consideration that tectonic activity is enclosed by other physical indicators, such as: geomorphic indicators, high degree of rock fracturation and high permeability areas, the integration of surveying techniques that focus the investigation from different and independent approaches—such as geophysical prospecting, trenching, fieldwork and aerial photography interpretation—may allow reducing considerably the degree of uncertainty.

Acknowledgments We would like to thank three anonymous reviewers for their very constructive comments and suggestions on the earlier version of this manuscript. The study has been partially financed by the Spanish Consejo de Seguridad Nacional project CSN2009-0001-C02-01and Education and Science Ministry (project CGL2005-02404). David Soler translated a first version of the manuscript.

References

Baubron JC, Rigo A, Toutain JP (2002) Soil gas profiles as a tool to characterise active tectonic areas: the Jaut Pass example (Pyrenees, France). Earth Planet Sci Lett 196:69–81

Beaubien SE, Ciotoli G, Lombardi S (2003) Carbon dioxide and radon gas hazard in the Alban Hills area (central Italy). J Volcanol Geothermal Res 123:63–80

Bisci C, Dramis F, SorrisoValvo M (1996) Rock flow (sackung). In: Dikau R et al (eds) Landslide recognition. Wiley, Chichester, pp 150–160

Caputo R, Salviulo L, Piscitelli S, Loperte A (2007) Late Quaternary activity along the Scorciabuoi fault (Southern Italy) as inferred from electrical resistivity tomographies. Ann Geophys 50: 213–224

Clever HL (1985) Solubility data series, vol 2, krypton-, xenon-, radon-gas solubilities. Pergamon Press, Oxford, pp 227–737

Colella A, Lapenna V, Rizzo E (2004) High-resolution imaging of the high agri valley basin (Southern Italy) with electrical resistivity tomography. Tectonophysics 386:29–40

Fazzito S, Rapalini A, Cortés JM, Terrizzano CM (2009) Characterization of Quaternary faults by electric resistivity tomography in the Andean Precordillera of Western Argentina. J South Am Earth Sci 28:217–228

Ferrer P, Masana E, Santanach P (1999) Geomorphological features of the Amer fault recent activity (NE Iberian Peninsula). Acta Geol Hisp 4:17–24

Fleta J, Santanach P, Goula X, Martínez P, Grellet B, Masana E (2001) Preliminary geologic, geomorphologic and geophysical studies for the paleoseismological analysis of the Amer fault (NE Spain). Neth J Geosci 80:243–253

Font Ll, Baixeras C, Moreno V, Bach J (2008) Soil radon levels across the Amer fault. Radiat Meas 43:S319–S323

Giammanco S, Imme G, Mangano G, Morelli D, Neri M (2009) Comparison between different methodologies for detecting radon in soil along an active fault: the case of the Pernicana fault system, Mt. Etna (Italy). Appl Radiat Isot 67:178–185

González-Díez A, Soto J, Gómez-Arozamena J, Bonachea J, Martínez-Díaz JJ, Cuesta JA, Olague I, Remondo J, Fernández Maroto G, Díaz de Terán JR (2009) Identification of latent faults using a radon test. Geomorphology 110:11–19

Guérin G, Benhamou G, Mallarach JM (1986) Un exemple de fusió parcial en medi continental. El vulcanisme quaternari de Catalunya. Vitrina 1:20–26

Gutiérrez-Santolalla F, Acosta E, Rios S, Guerrero J, Lucha P (2005) Geomorphology and geochronology of sackung features (uphill-facing scarps) in the Central Spanish Pyrenees. Geomorphology 69:298–314

Gutiérrez-Santolalla F, Ortuño M, Lucha P, Guerrero J, Acosta E, Coratza P, Piacentini D, Soldati M (2008) Late Quaternary episodic displacement on a sackung scarp in the central Spanish Pyrenees. Secondary paleoseismic evidence? Geodin Acta 21:187–202

Harvey AM (2002) Factors influencing the geomorphology of dry-region alluvial fans: a review. In: Pérez-González A, Vegas J, Machado MJ (eds) Aportaciones a la Geomorfología Española en el inicio del Tercer Milenio. Instituto Geológico y Minero de España, Madrid, pp 59–75

Hecht S (2003) Differentiation of loose sediments with seismic refraction methods—potentials and limitations derived from case studies. In: Schott L, Hordt A, Dikau R (eds) Geophysical applications in geomorphology. Annals of geomorphology, Supp vol 132, pp 89–102

Hofmann T, Schrott L (2003) Determining sediment thickness of talus slopes and valley fill deposits using seismic refraction—a comparison of 2D interpretation tools. In: Schott L, Hord A, Dikau R (eds) Geophysical applications in geomorphology. Annals of geomorphology, Supp vol 132, pp 71–87

ICC (1989) Mapa geològic de Catalunya 1:250.000. Institut Cartogràfic de Catalunya, Departament de Política Territorial i Obres Públiques de la Generalitat de Catalunya

ICC (1999) Mapa de sismicitat de Catalunya 1977–1997 1:400.000. Institut Cartogràfic de Catalunya, Departament de Política Territorial i Obres Públiques de la Generalitat de Catalunya

Igarashi G, Saeki S, Takahata N, Sumikawa K, Tasaka S, Sasaki Y, Takahashi M, Sano Y (1995) Ground-water radon anomaly before the Kobe earthquake in Japan. Science 269:60–61

Linares R, Pallí L, Roqué C, Vall E, Bascompte F, Oliveras J (2000) Aigües minerals (I). Termals i/o carbòniques. Cartografia temàtica de les terres gironines, 16, Universitat de Girona, Diputació de Girona 6, Direcció General d'Energia i Mines de la Generalitat de Catalunya

Linares R, Pallí L, Roqué C, Vall E (2001) Les manifestacions hidrotermals de les comarques gironines. Dialogant amb les pedres 9, Universitat de Girona

Linares R, Rosell J, Roqué C, Gutiérrez F (2010) Origin and evolution of tufa mounds related to artesian karstic springs in Isona area (Pyrenees. NE Spain). Geodin Acta 23:129–150

Loke MH (2000) Topographic modelling in resistivity imaging inversion, 62nd EAGE conference and technical exhibition extended abstracts, D-2

Loke MH (2011) Electrical imaging surveys for environmental and engineering studies—a practical guide to 2D and 3D surveys, Penang, Malaysia. http://www.geoelectrical.com/coursenotes.zip

Loke MH, Barker RD (1996) Rapid least-squares inversion of apparent resistivity pseudosections by a quasi-Newton method. Geophys Prospect 44:131–152

Louis I, Raftopoulos D, Goulis I, Louis F (2002) Geophysical imaging of faults and fault zones in the urban complex of Ano Liosia Nogene basin, Greece: synthetic simulation approach and field investigations. J Electr Electronics Eng Special Issue Oct 2002:269–285

McCalpin JP (2009) Field techniques in paleoseismology–terrestrial environments. In: McCalpin JP (ed) Paleoseismology. Academic Press, San Diego, pp 29–117

Moreno V, Baixeras C, Font Ll, Bach J (2008) Indoor radon levels and their dynamics in relation with the geological characteristics of La Garrotxa, Spain. Radiat Meas 43:1532–1540

Moreno V, Bach J, Baixeras C, Ll Font (2009) Characterization of blowholes as radon and thoron sources in the volcanic region of La Garrotxa, Spain. Radiat Meas 44:929–933

Nguyen F, Garambois S, Chardon D, Hermitte D, Bellier O, Jongmans D (2007) Subsurface electrical imaging of anisotropic formations affected by a slow active reverse fault, Provence, France. J Appl Geophys 62:338–353

Olivera C, Redondo E, Lambert J, Riera A, Roca A (2006) Els terratrèmols dels segles XIV i XV a Catalunya. Institut Cartogràfic de Catalunya, Barcelona

Perea H (2009) The Catalan seismic crisis (1427 and 1428; NE Iberian Peninsula): geological sources and earthquake triggering. J Geodyn 47:259–270

Puig C, Mató E, Saula E, Picart J, Solà J, Montaner J, Mallarach J, Samsó J, Serra J (1997) Mapa geològic de Catalunya 1:25.000 Amer 295-1-2 (75-24). Institut Cartogràfic de Catalunya, Servei Geològic de Catalunya, Departament de Política Territorial i Obres Públiques de la Generalitat de Catalunya

Purtscheller F, Pirchl T, Sieder G, Stingl V, Tessadri T, Brunner P, Ennemoser O, Schneider P (1995) Radon emanation from giant landslides of Koefels (Tyrol, Austria) and Langtang Himal (Nepal). Environ Geol 26:32–38

Redondo R, Yélamos JG (2000) Hidrogeoquímica convencional e isotópica de las aguas carbónicas de Cataluña. Geogaceta 28:121–124

Redondo R, Yélamos JG (2005) Determination of CO_2 origin (natural or industrial) in sparkling bottled waters by 13C/12C isotope ratio analysis. Food Chem 92:507–514

Richon P, Klinger Y, Tapponnier P, Li ChX, Van Der Woerd J, Perrier F (2010) Measuring radon flux across active faults: relevance of excavating and possibility of satellite discharges. Radiat Meas 45:211–218

Rizzo E, Colella A, Lapenna V, Piscitelli S (2004) High-resolution images of the fault controlled High Agri Valley basin (Southern Italy) with deep and shallow electrical resistivity tomographies. Phys Chem Earth 29:321–327

Saula E, Picart J, Mató E, Llenas M, Losantos M, Berástegui X, Agustí J (1996) Evolución geodinámica de la fosa del Empordà y las Sierras Transversales. Acta Geol Hisp 29:55–75

Scott J (1973) Seismic refraction modeling by computer. Geophysics 38:271–284

Seminsky KZh, Bobrov AA (2009) Radon activity of faults (western Baikal and southern Angara areas). Russ Geol Geophys+ 5:682–692

Soldati M (2004) Deep-seated gravitational slope deformation. In: Goudie AS (ed) Encyclopedia of geomorphology, vol 1. Routledge, New York, pp 226–228

Spiegel RJ, Sturdivant VR, Owen TE (1980) Modeling resistivity anomalies from localized voids under irregular terrain. Geophysics 45:1164–1183

Suski B, Brocard G, Authemayou C, Muralles BC, Teyssier C, Holliger K (2010) Localization and characterization of an active fault in an urbanized area in central Guatemala by means of geoelectrical imaging. Tectonophysics 480:88–98

Toutain JP, Baubron JC (1999) Gas geochemistry and seismotectonics: a review. Tectonophysics 304:1–27

Tuccimei P, Soligo M (2008) Correcting for CO_2 interference in soil radon flux measurements. Radiat Meas 43:102–105

Vanneste K, Verbeeck K, Petermans T (2008) Pseudo-3D imaging of a low-slip-rate, active normal fault using shallow geophysical methods: the Geleen fault in the Belgian Maas River valley. Geophysics 73. doi:10.1190/1.2816428

Wattananikorn K, Kanaree M, Wiboolsake S (1998) Soil gas radon as an earthquake precursor: some considerations on data improvement. Radiat Meas 29:593–598

Wilhelm E, Battino R, Wilcock RJ (1977) Low-pressure solubility of gases in liquid water. Chem Rev 77:219–262

Zhu T, Feng R, Hao J, Zhou J, Wang H, Wang S (2009) The application of electrical resistivity tomography to detecting a buried fault: a case study. J Environ Eng Geophys 14:145–151

Zischinsky U (1969) Über Sackungen. Rock Mech 1:30–52